Femtosecond energy- and angle-resolved photoelectron spectroscopy

Yasuki Arasaki and Kazuo Takatsuka[a)]
Department of Basic Science, Graduate School of Arts and Sciences, University of Tokyo, Komaba, 153-8902, Tokyo, Japan

Kwanghsi Wang and Vincent McKoy
Laboratory for Molecular Sciences, California Institute of Technology, Pasadena, California 91125

(Received 10 January 2000; accepted 28 February 2000)

We present a formulation of energy- and angle-resolved photoelectron spectra for femtosecond pump–probe ionization of wave packets and results of its application to the $^1\Sigma_u^+$ double-minimum state of aligned Na_2. The formulation is well-suited for inclusion of the underlying dynamics of molecular photoionization and its dependence on molecular geometry. Results are presented for three typical pump laser energies selected so as to investigate qualitatively different patterns of the spatio-temporal propagation of wave packets on the double-minimum potential curve and of their associated photoelectron spectra. Photoelectron angular distributions are also reported for different orientations of linearly polarized pump and probe pulses. The resulting photoelectron spectra illustrate the importance of a proper description of the underlying photoionization amplitudes and their dependence on geometry for unraveling wave packet dynamics from pump–probe photoelectron signals in nonadiabatic regions where the electronic structure evolves rapidly with geometry. The dependence of these photoelectron angular distributions on relative orientation of the molecule and polarization of the probe pulse are also seen to be potentially useful for real-time monitoring of molecular rotation. © *2000 American Institute of Physics.* [S0021-9606(00)00720-0]

I. INTRODUCTION

With femtosecond (fs) laser techniques it is now possible to observe nuclear dynamics and to chart the path of chemical reactions in real time.[1–3] Femtosecond time-resolved spectroscopy has been exploited in numerous applications ranging from fundamental studies of real-time motion in the photodissociation dynamics of NaI to studies of electron transfer in biological systems.[1–5] In femtosecond spectroscopy, a pump pulse prepares an initial wave packet which evolves in accordance with the time scales for vibrational ($\sim 10^{-13}$ s) and rotational ($\sim 10^{-10}$ s) motion. The evolution of the wave packet is then probed by a time-delayed, probe pulse via excitation to a final state. Several techniques using different types of final states have been used to probe these wave packets.[1,2,6,7] These include the use of absorption, laser-induced fluorescence, multiphoton ionization, photoelectron spectroscopy, nonlinear degenerate four-wave mixing, time-resolved mass spectroscopy, and stimulated emission pumping.

Time-resolved ionization offers several advantages as a probe of these wave packets.[8–11] For example, the ground state of an ion is often better characterized than higher excited states of the neutral molecule, particularly for polyatomics. Ionization is also universal and hence there are no dark states. Furthermore, ionization provides both ions and photoelectrons and, while ion detection provides mass and kinetic-energy resolution in time-resolved studies,[12] photoelectron spectra can provide complementary information on the evolution of the wave packet.[13–22] Its utility for real-time probing of molecular dynamics in the femtosecond regime has been nicely demonstrated in studies of wave packets on excited states of Na_2,[19] on the B state of I_2,[20] and on the A state of NaI.[21,22] Furthermore, Davies *et al.*[23] have recently reported the first femtosecond photoelectron–photoion coincidence imaging studies of photodissociation dynamics.

Many of these studies of femtosecond photoelectron spectra were stimulated by the seminal papers of Engel and co-workers[16–18] which illustrated how well-suited photoelectron distributions from pump–probe ionization at various delay times are for mapping wave packet motion in diatomics. While these studies and those of Charron and Suzor-Weiner[22] have clearly served to illustrate the utility and promise of photoelectron spectroscopy for real-time mapping of wave packet dynamics in small molecular systems, they have generally ignored any dependence of the underlying photoionization amplitudes on geometry[24] and energy in their studies of the energy distributions of the photoelectrons. Neglecting the dependence of the photoionization matrix element on geometry is a poor approximation when the wave packet moves through a region of an avoided crossing where the electronic character of the wave function changes dramatically. In such regions, knowledge of the underlying photoionization dynamics is essential in unraveling the wave packet dynamics from the probe signal. Both the double-minimum state of Na_2 studied by Engel and co-workers[16–18] and the A state of NaI studied by Charron and Suzor-Weiner[22] are, in fact, formed by an avoided cross-

a)Author to whom correspondence should be addressed; electronic mail: kaztak@mns2.c.u-tokyo.ac.jp

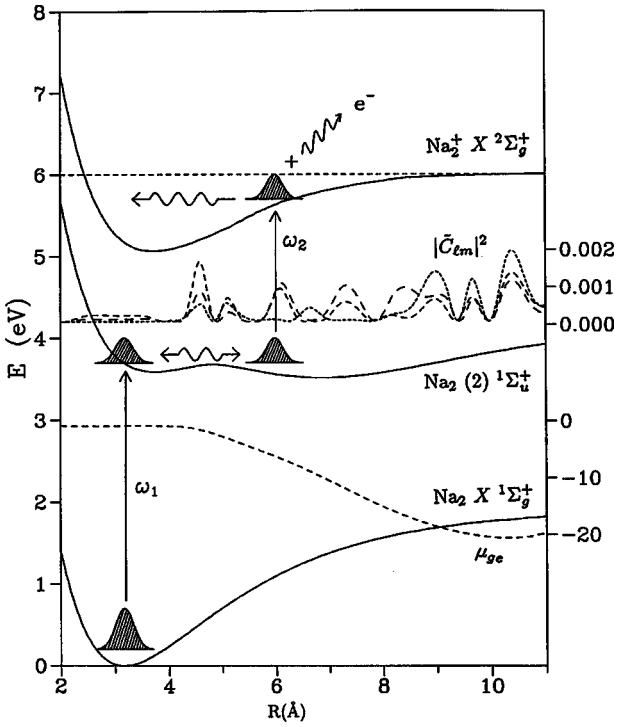

FIG. 1. Potential curves for the $X\ ^1\Sigma_g^+$ and (2) $^1\Sigma_u^+$ states of Na_2 and the $X\ ^2\Sigma_g^+$ state of Na_2^+. The dipole amplitude (μ_{ge}) and photoionization coefficients ($\tilde{C}_{\ell m}$) for the molecule parallel to the pump and probe fields are also shown for a kinetic energy of 0.5967 eV. The partial waves $\ell=0$, 2, and 4 with $m=0$ are denoted by long, medium, and short dashed lines, respectively.

ing of two diabatic states. Furthermore, these studies[16–18,22] did not examine photoelectron angular distributions which can be expected to convey richer structural and dynamical information than is contained in angle-averaged energy spectra.[23,25,26]

We have recently published a brief report[27] on the results of detailed quantum-mechanical studies of energy- and angle-resolved pump-probe femtosecond photoelectron spectra for the $^1\Sigma_u^+$ double-minimum state of the Na_2 molecule. In this paper we present a full account of the basic formulation and technique used in this study, along with more detailed results of these femtosecond photoelectron spectra of the $^1\Sigma_u^+$ double-minimum state of aligned Na_2 molecules. In these studies we employ geometry- and energy-dependent photoionization amplitudes derived from calculations employing sophisticated descriptions of the wave functions for the double-minimum state and for the molecular photoelectron. To illustrate the utility of femtosecond photoelectron spectra for probing both molecular vibrations and rotations in real time, we also report spectra for molecules aligned via a linearly polarized pump pulse and ionized by a probe pulse polarized either parallel or perpendicular to the pump pulse.

This paper is organized as follows. In Sec. II we present the quantum-mechanical formulation employed in these studies of energy- and angle-resolved photoelectron spectra, and some methodological issues associated with the formulation and practical techniques devised to address them. Results of a case study of the $^1\Sigma_u^+$ double-minimum state for aligned Na_2 are then presented in the remaining sections. In

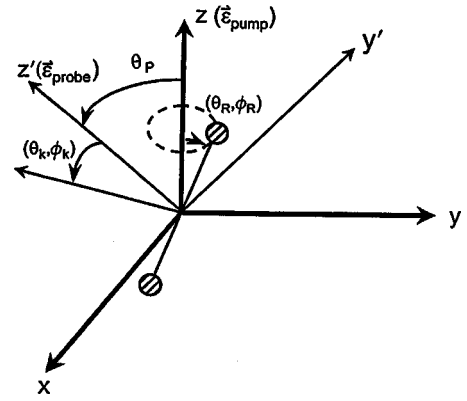

FIG. 2. Orientation of the molecule and pump and probe laser fields: molecular orientation angles (θ_R, ϕ_R) are specified in the pump frame and photoelectron angles (θ_k, ϕ_k) in the probe frame.

Sec. III we discuss a few relevant aspects of the electronic wave functions and photoionization amplitudes used here, while in Sec. IV we present the wave packet dynamics associated photoelectron spectra of these studies. The paper concludes with a few remarks in Sec. V.

II. FORMULATION

Figure 1 illustrates the scheme used in our studies of the femtosecond energy- and angle-resolved photoelectron spectra for vibrational wave packets in the $^1\Sigma_u^+$ double-minimum state of aligned Na_2 molecules. A linearly polarized laser pulse of frequency ω_1 prepares a wave packet on the double-minimum $^1\Sigma_u^+$ state, which is then ionized by a time-delayed linearly polarized laser pulse of frequency ω_2. Figure 2 illustrates the relevant coordinate frames. The molecule is oriented at angles (θ_R, ϕ_R) with respect to the polarization vector of the pump pulse and the photoelectron angular distributions (θ_k, ϕ_k) are measured relative to the polarization vector of the probe pulse. The angle between the probe and pump vectors is θ_P and, without loss of generality, the probe is assumed to lie in the *xz* plane of the pump frame. In the dipole approximation the interaction between the laser fields and the molecule is given by

$$\begin{aligned} V(t) &= V_1(t) + V_2(t;\Delta T) \\ &= E_{01} f_1(t) \sin(\omega_1 t)\, \boldsymbol{\varepsilon}_{\text{pump}} \cdot \mathbf{d} \\ &\quad + \tfrac{1}{2} E_{02} f_2(t-\Delta T) \exp(-i\omega_2 (t-\Delta T))\, \boldsymbol{\varepsilon}_{\text{probe}} \cdot \mathbf{d}, \end{aligned} \tag{1}$$

where V_1 and V_2 represent the pump and probe fields, respectively, and, although more general forms can be readily assumed, we have made the rotating wave approximation in V_2. E_{01} and E_{02} are the field amplitudes, $f_1(t)$ and $f_2(t-\Delta T)$ are Gaussian envelope functions, ΔT is the delay time between the two lasers, $\boldsymbol{\varepsilon}_{\text{pump}}$ and $\boldsymbol{\varepsilon}_{\text{probe}}$ are the polarization vectors, and $\mathbf{d}$ is the electric dipole operator. Generally, the time scale of the rotational motion (of the order 10^{-10} sec) is two or three orders of magnitude slower than that of molecular vibrations (with a typical period of 10^{-13} sec). The pump pulse produces a polarized distribu-

tion of molecules with a $\cos^2\theta_R$ dependence with respect to $\boldsymbol{\varepsilon}_{\text{pump}}$.[28] The probe laser with a pulse width of ~100 fs will probe this aligned distribution of slowly rotating molecules.

The Schrödinger equation can be written as

$$i\hbar\frac{\partial}{\partial t}\Psi(t)=[T_N+H_{\text{el}}+V(t)]\Psi(t), \tag{2}$$

where T_N is the nuclear kinetic energy operator and H_{el} is the electronic Hamiltonian. The time-dependent total wave function is expanded as

$$\Psi(\mathbf{r},R,t)=\chi_g(R,t)\Phi_g(\mathbf{r};R)+\chi_e(R,t)\Phi_e(\mathbf{r};R)+\int d\mathbf{k}\chi_{\mathbf{k}}(R,t)\Phi_{\mathbf{k}}^{(-)}(\mathbf{r};R), \tag{3}$$

where Φ_g, Φ_e, and $\Phi_{\mathbf{k}}^{(-)}$ are eigenfunctions of H_{el} representing the ground, excited, and ion states, respectively, $\mathbf{r}$ denotes the electronic coordinates, and R the internuclear distance. Molecular rotation can be explicitly included in Eq. (3) by replacing R by $\mathbf{R}$. The functions, χ_g, χ_e, and $\chi_{\mathbf{k}}$ are wave packets on the individual potential surfaces. Unlike excitation to a bound state, the final states in Eq. (3), $\chi_{\mathbf{k}}$, are characterized by photoelectron energies and angles, which eventually constitute an infinitely many channel problem. Expansion of the continuum part of $\Psi(\mathbf{r},R)$ in spherical harmonics leads to

$$\Psi(\mathbf{r},R,t)=\chi_g(R,t)\Phi_g(\mathbf{r};R)+\chi_e(R,t)\Phi_e(\mathbf{r};R)+\int dk k^2\sum_{\ell m}(-1)^m\chi_{k\ell m}(R,t)\Phi_{k\ell -m}^{(-)}\times(\mathbf{r};R), \tag{4}$$

where we have assumed the following expansions of $\Phi_k^{(-)}$ and $\chi_{\mathbf{k}}$ in spherical harmonics, $Y_{\ell m}(\hat{k})$, with $\hat{k}$ measured with respect to the probe,

$$\Phi_{\mathbf{k}}^{(-)}(\mathbf{r};R)=\sum_{\ell m}\Phi_{k\ell m}^{(-)}(\mathbf{r};R)Y_{\ell m}(\hat{k}) \tag{5}$$

and

$$\chi_{\mathbf{k}}(R,t)=\sum_{\ell m}\chi_{k\ell m}(R,t)Y_{\ell m}(\hat{k}). \tag{6}$$

The electronic eigenfunctions provide the potential curves for the ground, excited, and ionic states, respectively,

$$H_{\text{el}}\Phi_g(\mathbf{r};R)=V_g(R)\Phi_g(\mathbf{r};R), \tag{7}$$

$$H_{\text{el}}\Phi_e(\mathbf{r};R)=V_e(R)\Phi_e(\mathbf{r};R), \tag{8}$$

and

$$H_{\text{el}}\Phi_{\mathbf{k}}^{(-)}(\mathbf{r};R)=\left[V_{\text{ion}}(R)+\frac{(k\hbar)^2}{2m_e}\right]\Phi_{\mathbf{k}}^{(-)}(\mathbf{r};R), \tag{9}$$

where m_e is the electron mass. The $(-)$ sign on the continuum electronic wave function $\Phi_{\mathbf{k}}^{(-)}$ indicates the so-called incoming-wave boundary condition, which is canonically used to represent dissociation (ejection) in stationary-state scattering theory. Calculation of $\Phi_{\mathbf{k}}^{(-)}$ is challenging and will be discussed in detail later. These electronic eigenfunctions are orthogonal to each other. In particular, we impose the delta-function type orthonormal condition

$$\langle\Phi_{\mathbf{k}_1}^{(-)}|\Phi_{\mathbf{k}_2}^{(-)}\rangle=\delta(\mathbf{k}_1-\mathbf{k}_2) \tag{10}$$

on the continuum functions.

Finally, we note the possibility that the upper bound for the integration over $\mathbf{k}$ in Eq. (3) can, in principle, exceed those values limited by the total energies of the pump and probe lasers. This arises not only from the energy width associated with the laser pulses due to the uncertainty principle, but from energetically closed channels required in the expansion of Eq. (3) to represent the deformation (polarization in the terminology of scattering theory) of both electronic and nuclear states.

A. Equations of motion for nuclear wave packets

The equations of motion for the nuclear wave packets are obtained as usual by projecting $\langle\Phi_g(R)|_{\mathbf{r}}$, $\langle\Phi_e(R)|_{\mathbf{r}}$, and $\langle\Phi_{\mathbf{k}}^{(-)}(R)|_{\mathbf{r}}$ (integrate over $\mathbf{r}$) onto the total Schrödinger equation. The resulting coupled equations are

$$i\hbar\frac{\partial}{\partial t}\chi_g(R,t)=[T_N+V_g(R)]\chi_g(R,t)+\langle\Phi_g(R)|V_1(t)|\Phi_e(R)\rangle\chi_e(R,t), \tag{11}$$

$$i\hbar\frac{\partial}{\partial t}\chi_e(R,t)=[T_N+V_e(R)]\chi_e(R,t)+\langle\Phi_e(R)|V_1(t)|\Phi_g(R)\rangle\chi_g(R,t)+\int d\mathbf{k}\langle\Phi_e(R)|V_2(t;\Delta T)|\Phi_{\mathbf{k}}^{(-)}(R)\rangle\times\chi_{\mathbf{k}}(R,t), \tag{12}$$

and

$$i\hbar\frac{\partial}{\partial t}\chi_{\mathbf{k}}(R,t)=\left[T_N+V_{\text{ion}}(R)+\frac{(k\hbar)^2}{2m_e}\right]\chi_{\mathbf{k}}(R,t)+\langle\Phi_{\mathbf{k}}^{(-)}(R)|V_2(t;\Delta T)|\Phi_e(R)\rangle\times\chi_e(R,t), \tag{13}$$

respectively. In deriving these, we have used the orthogonality conditions among the electronic eigenfunctions stated above and imposed the following conditions:

(a) adiabaticity of the bound electronic wave functions, i.e.,

$$\langle\Phi_g(R)|T_N|\Phi_e(R)\rangle_{\mathbf{r}}\cong 0,$$

(b) adiabaticity of the continuum functions,

$$\int d\mathbf{k}'\langle\Phi_{\mathbf{k}}^{(-)}|T_N|\Phi_{\mathbf{k}'}^{(-)}\rangle|\chi_{\mathbf{k}'}\rangle\cong\int d\mathbf{k}'\langle\Phi_{\mathbf{k}}^{(-)}|\Phi_{\mathbf{k}}^{(-)}\rangle T_N|\chi_{\mathbf{k}'}\rangle=T_N|\chi_{\mathbf{k}}\rangle,$$

(c) the matrix elements of $V_2(t)$ between continuum functions are all zero, i.e.,

$$\langle \Phi_{\mathbf{k}_1}^{(-)} | V_2(t;\Delta T) | \Phi_{\mathbf{k}_2}^{(-)} \rangle_{\mathbf{r}} \cong 0.$$

The nonadiabatic coupling between the ground and excited states will be taken into account explicitly in a future publication on the NaI system.[29]

Using the expansions of $\Phi_{\mathbf{k}}^{(-)}$ and $\chi_{\mathbf{k}}$ in Eqs. (5) and (6), Eqs. (12) and (13) can be written

$$\begin{aligned} i\hbar \frac{\partial}{\partial t}\chi_e(R,t) = & [T_N + V_e(R)]\chi_e(R,t) \\ & + \langle \Phi_e(R) | V_1(t) | \Phi_g(R) \rangle \chi_g(R,t) \\ & + \int k^2 dk \sum_{\ell m} (-1)^m \langle \Phi_e(R) | \\ & \times V_2(t;\Delta T) | \Phi_{k\ell -m}^{(-)}(R) \rangle \chi_{k\ell m}(R,t) \end{aligned} \quad (14)$$

and

$$\begin{aligned} i\hbar \frac{\partial}{\partial t}\chi_{k\ell m}(R,t) = & \left[T_N + V_{\text{ion}}(R) + \frac{(k\hbar)^2}{2m_e} \right] \chi_{k\ell m}(R,t) \\ & + (-1)^m \langle \Phi_{k\ell -m}^{(-)}(R) | V_2(t;\Delta T) | \Phi_e(R) \rangle \\ & \times \chi_e(R,t). \end{aligned} \quad (15)$$

The equations of motion are now in the form of coupled equations specified in terms of a set of indices (g, e, k, ℓ, m).

B. Transition amplitudes

The dipole interaction between the ground and excited states becomes

$$\langle \Phi_e | V_1(t) | \Phi_g \rangle = -E_{01} f_1(t) \sin(\omega_1 t) d_{eg} \cos(\theta_R), \quad (16)$$

with d_{eg} the magnitude of the dipole moment. Hence, under a sufficiently weak field, where the Rabi oscillation is suppressed, the distribution of molecular orientation in the excited state is proportional to $\cos^2(\theta_R)$.

The photoionization matrix elements constitute a key quantity in the present study. To obtain these matrix elements we write $\Phi_{\mathbf{k}}^{(-)}$ as an antisymmetrized product of an ion wave function, Φ_+, and a photoelectron orbital, $\phi_{\mathbf{k}}^{(-)}$,

$$\Phi_{\mathbf{k}}^{(-)} = \mathcal{A}(\Phi_+ \cdot \phi_{\mathbf{k}}^{(-)}), \quad (17)$$

where

$$\phi_{\mathbf{k}}^{(-)} = \sum_{\ell,m,\lambda} i^{\ell} e^{-i\eta_\ell} \mathcal{D}^{\ell}_{\lambda m}(\hat{R}') Y^*_{\ell m}(\hat{k}) \psi_{k\ell\lambda}^{(-)}(\mathbf{r}';R), \quad (18)$$

with $\mathbf{r}'$ being the electronic coordinate vector in the molecular frame. In Eq. (18) $\psi_{k\ell\lambda}^{(-)}$ is a partial-wave component of the photoelectron orbital in the molecular frame with momentum $\mathbf{k}$, λ is the projection of ℓ in the molecular frame, $\mathcal{D}^{\ell}_{\lambda m}$ transforms the molecular-frame wave functions to those in the laboratory (probe) frame, and η_ℓ is the Coulomb phase shift.[30]

Photoelectron detection is, of course, with respect to the polarization vector of the probe laser. The dipole operator is hence given by

$$D_{\mu 0} = \sqrt{\frac{4\pi}{3}} r \sum_{\mu} \mathcal{D}^1_{\mu\mu_0}(\hat{R}') Y_{1\mu}(\hat{r}') \quad (19)$$

in the probe laser frame. The interaction V_2 between the probe laser and the molecule becomes

$$V_2 = \tfrac{1}{2} E_{02} \cdot f_2(t-\Delta T) \exp(-i\omega_2(t-\Delta T)) D_{\mu_0}, \quad (20)$$

and the coupling matrix element between the excited state Φ_e and the final ionized state can be written as

$$\begin{aligned} & \langle \Phi_{\mathbf{k}}^{(-)}(R) | V_2(t;\Delta T) | \Phi_e(R) \rangle \\ & = \tfrac{1}{2} E_{02} \cdot f_2(t-\Delta T) \exp(-i\omega_2(t-\Delta T)) \\ & \quad \times \sum_{\ell m} C_{\ell m} Y_{\ell m}(\hat{k}), \end{aligned} \quad (21)$$

$$\begin{aligned} & C_{\ell m}(k,\theta_R,\phi_R,\theta_P) \\ & = \sqrt{\frac{4\pi}{3}} \sum_{\lambda\mu} I_{\ell\lambda\mu} \mathcal{D}^{\ell *}_{\lambda m}(\hat{R}') \mathcal{D}^1_{\mu\mu_0}(\hat{R}'). \end{aligned} \quad (22)$$

$I_{\ell\lambda\mu}$ is a partial-wave matrix element in the molecular frame. These are formed from dipole matrix elements between $|\Phi_+ \psi_{k\ell\lambda}^{(-)}\rangle$ and the components of the CI wave function used to describe Φ_e. For the case of ionization of an orbital ϕ_i into $\psi_{k\ell\lambda}^{(-)}$ these assume the form

$$\begin{aligned} & I^{(0)}_{\ell\lambda\mu}(R) \\ & = (-i)^{\ell} e^{i\eta_\ell} \sum_{\ell_0\lambda_0} \langle \psi_{k\ell\lambda}^{(-)} | r Y_{1\mu}(\hat{r}') | \phi_{i,\ell_0\lambda_0}(r) Y_{\ell_0\lambda_0}(\hat{r}') \rangle. \end{aligned} \quad (23)$$

These $C_{\ell m}$ coefficients provide the underlying dynamical information needed to describe the photoionization of an oriented Na_2 molecule by the probe laser. The angular momentum coupling inherent in molecular photoelectrons can be seen in a single-center expansion of $\psi_{k\ell\lambda}$ for a linear molecule

$$\psi_{k\ell\lambda}^{(-)}(\mathbf{r},R) = \sum_{\ell'} g^{(-)}_{\ell\ell'\lambda}(k,r,R) Y_{\ell'\lambda}. \quad (24)$$

Use of photoelectron orbitals which correctly incorporate such angular momentum coupling is essential for a quantitative description of molecular photoionization.

The Euler angles in Eq. (22) are easily determined by considering an intermediate ''pump frame,'' and combining the two Euler angles for the pump-to-molecule frame $\mathcal{D}(\phi_R,\theta_R,\gamma_R)$ and the pump-to-probe frame $\mathcal{D}(0,\theta_P,0)$.[31] The two sets of the Euler angles define the molecular and probe frames with respect to the pump frame. Here the pump and probe polarization vectors lie on the positive z-axis of each respective frame. Without loss of generality, the probe frame z-axis is chosen to be on the pump frame xz-plane so that a single angle θ_P conveniently describes the relation of the probe frame to the pump frame (see Fig. 2). The molecule can be oriented in any manner with respect to the pump and probe polarization vectors. For the case of a linear molecule γ_R is arbitrary and we simply choose it to be zero. Combining the rotation from the molecular frame to the

pump frame and that from the pump frame to the probe frame, the rotation from the molecular frame to the probe frame can be written explicitly as a sequence of rotations about successively defined axes

$$\mathcal{D}(\alpha\beta\gamma)=\mathcal{D}(0,\theta_P,0)\mathcal{D}(-\gamma_R,-\theta_R,-\phi_R). \tag{25}$$

Writing out both sides of Eq. (25) as Cartesian rotation matrices results in a set of equations that determine the Euler angles α, β, and γ.

To obtain the final state wave functions needed in evaluating the photoelectron matrix elements, we assume a frozen-core Hartree–Fock model in which the core orbitals are taken to be those of the ion and the photoelectron orbital is obtained as a solution of a one-electron Schrödinger equation containing the Hartree–Fock potential of the molecular ion, $V_{\rm ion}(\mathbf{r},R)$, i.e.,

$$\left(-\frac{\hbar^2}{2m_e}\nabla^2+V_{\rm ion}(\mathbf{r},R)-\frac{(k\hbar)^2}{2m_e}\right)\psi^{(-)}_{k\ell m}(\mathbf{r},R)=0. \tag{26}$$

To obtain the partial-wave photoelectron orbitals $\psi^{(-)}_{k\ell m}$, we use an iterative procedure, based on the Schwinger variational principle, to solve the Lippmann–Schwinger equation associated with Eq. (26).[30] This procedure begins by approximating the static-exchange potential of the relaxed ion core by a separable form

$$U_{SE}\approx U_S(\mathbf{r},\mathbf{r}')=\sum_{i,j}\langle\mathbf{r}|U|\alpha_i\rangle(U^{-1})_{ij}\langle\alpha_j|U|\mathbf{r}'\rangle, \tag{27}$$

where the matrix U^{-1} is the inverse of the matrix with the elements $(U)_{ij}=\langle\alpha_i|U|\alpha_j\rangle$, the α's are discrete basis functions such as Cartesian or spherical Gaussian functions, and U is twice the static-exchange potential in Eq. (26) with the long-range Coulomb potential removed. The Lippmann–Schwinger equation with this separable potential $U_S(\mathbf{r},\mathbf{r}')$ can be readily solved and provides an approximate photoelectron orbital $\psi^{(0)}_{k\ell m}$. These solutions can be iteratively improved to yield converged solutions to the Lippmann–Schwinger equation containing the exact static-exchange potential U_{SE}. Usually, several iterations will provide converged solutions of Eq. (26).

Insertion of Eqs. (16) and (21) into Eqs. (14) and (15) yields the following equations of motion for the nuclear wave packets:

$$i\hbar\frac{\partial}{\partial t}\chi_g(R,t)=[T_N+V_g]\chi_g(R,t)+V_{ge}\chi_e(R,t), \tag{28}$$

$$\begin{aligned}i\hbar\frac{\partial}{\partial t}\chi_e(R,t)&=[T_N+V_e]\chi_e(R,t)+V_{eg}\chi_g(R,t)\\&\quad+\frac{1}{2}\int dk k^2\sum_{\ell m}E_{02}f_2(t-\Delta T)\\&\quad\times\exp(i\omega_2(t-\Delta T))C^*_{\ell m}(k,\theta_R,\phi_R,\theta_P)\\&\quad\times\chi_{k\ell m}(R,t),\end{aligned} \tag{29}$$

and

$$\begin{aligned}&i\hbar\frac{\partial}{\partial t}\chi_{k\ell m}(R,t)\\&\quad=\left[T_N+V_{\rm ion}+\frac{(k\hbar)^2}{2m_e}\right]\chi_{k\ell m}(R,t)\\&\qquad+\tfrac{1}{2}E_{02}f_2(t-\Delta T)\exp(-i\omega_2(t-\Delta T))\\&\qquad\times C_{\ell m}(k,\theta_R,\phi_R,\theta_P)\chi_e(R,t).\end{aligned} \tag{30}$$

In Eqs. (28) and (29), $V_{eg}=\langle\Phi_e|V_1(t)|\Phi_g\rangle$ and V_{ge} its complex conjugate.

C. Solution of the coupled equations

Discretization of the continuum integration in Eq. (29) via a finite quadrature such as Gauss–Legendre quadrature leads to

$$\begin{aligned}i\hbar\frac{\partial}{\partial t}\chi_e(R,t)&=[T_N+V_e]\chi_e(R,t)+V_{eg}\chi_g(R,t)\\&\quad+\frac{1}{2}\sum_{j=1}^{N_k}\sum_{\ell m}E_{02}k_j^2w_jf_2(t-\Delta T)\\&\quad\times\exp(i\omega_2(t-\Delta T))C^*_{\ell m}(k_j,\theta_R,\phi_R,\theta_P)\\&\quad\times\chi_{k_j\ell m}(R,t),\end{aligned} \tag{31}$$

where N_k is the number of the quadrature points and w_j are the weights. This discretization leads to a finite set of coupled equations of motion.[14] However, the hermiticity of the transition matrix is broken in the resultant coupled equations, which can result in numerical instability and a loss of norm. To remedy this situation, we redefine the wave packets and matrix elements as

$$\tilde{\chi}_{k_j\ell m}(R,t)=k_j\sqrt{w_j}\chi_{k_j\ell m}(R,t) \tag{32}$$

and

$$\tilde{C}_{\ell m}(k_j,\theta_R,\phi_R,\theta_P)=k_j\sqrt{w_j}C_{\ell m}(k_j,\theta_R,\phi_R,\theta_P), \tag{33}$$

and rewrite the equations of motion as

$$\begin{aligned}i\hbar\frac{\partial}{\partial t}\chi_e(R,t)&=[T_N+V_e]\chi_e(R,t)+V_{eg}\chi_g(R,t)\\&\quad+\frac{1}{2}\sum_{j=1}^{N_k}\sum_{\ell m}E_{02}f_2(t-\Delta T)\exp(i\omega_2(t\\&\quad-\Delta T))\tilde{C}^*_{\ell m}(k_j,\theta_R,\phi_R,\theta_P)\tilde{\chi}_{k_j\ell m}(R,t),\end{aligned} \tag{34}$$

and

$$\begin{aligned}i\hbar\frac{\partial}{\partial t}\tilde{\chi}_{k_j\ell m}(R,t)&=\left[T_N+V_{\rm ion}+\frac{(k_j\hbar)^2}{2m_e}\right]\tilde{\chi}_{k_j\ell m}(R,t)\\&\quad+\tfrac{1}{2}E_{02}f_2(t-\Delta T)\exp(-i\omega_2(t-\Delta T))\\&\quad\times C^*_{\ell m}(k_j,\theta_R,\phi_R,\theta_P)\chi_e(R,t).\end{aligned} \tag{35}$$

It is readily seen that the hermiticity has been recovered. The normalization of the scattering part of the total wave function now becomes

$$\left\langle \int \Phi_{\mathbf{k}_1}^{(-)}\chi_{\mathbf{k}_1}d\mathbf{k}_1 \middle| \int \Phi_{\mathbf{k}_2}^{(-)}\chi_{\mathbf{k}_2}d\mathbf{k}_2 \right\rangle = \int d\mathbf{k}\langle\chi_{\mathbf{k}}|\chi_{\mathbf{k}}\rangle \cong \sum_{j=1}^{N_k}\sum_{\ell m}\langle\tilde{\chi}_{k_j\ell m}|\tilde{\chi}_{k_j\ell m}\rangle. \tag{36}$$

The total wave function of Eq. (3) should display only spherical outgoing waves in the asymptotic region in electronic coordinates in the remote future, since it is designed to describe a photoionization process. Nonetheless, $\Psi(\mathbf{r},R,t)$ can be contaminated by the (electronic) spherical incoming waves in the asymptotic region. This is because $\Phi_{\mathbf{k}}^{(-)}(\mathbf{r};R)$ is an eigenfunction of the electronic Hamiltonian having a real-valued energy and hence is composed of both spherical incoming and outgoing waves in the asymptotic region. The incoming spherical wave represents electronic recombination with photon emission, whose probability must be negligibly small in our system. As soon as the ionized state is formed by photoabsorption, an electron is ejected much faster—within a few femtoseconds—than the time scale of molecular vibration. This emission of the photoelectron should be irreversible. However, our coupled equations do allow for the reverse process: photoemission by the electron recaptured by the ion, which is mathematically analogous to the Raman–Stokes deactivation. One needs to address this issue of time irreversibility and the outgoing boundary condition.

We first consider why $\Phi_{\mathbf{k}}^{(-)}(\mathbf{r};R)$ is an adequate basis in the expansion of Eq. (3). For a general half-collision problem (ionization in this particular case) due to a stationary optical source, the time-independent coupled Schrödinger equations can be written as

$$(E-H_i)\,\phi_i = V^*\phi_f \tag{37}$$

and

$$(E-H_f)\,\phi_f = V\phi_i, \tag{38}$$

where the latter represents a dissociative process due to optical pumping from a bound state ϕ_i, while the former describes the reverse process of deactivation from ϕ_f to ϕ_i. Provided a continuum eigenfunction in Eq. (38) satisfies incoming boundary conditions, i.e.,

$$(E-H_f)\lambda_f^{(-)}(E)=0, \tag{39}$$

it is well-known that

$$T_{if}=\langle\lambda^{(-)}(E)|V|\phi_i(0)\rangle \tag{40}$$

gives a transition amplitude for this dissociative event, where $\phi_i(0)$ is an unperturbed state before photoabsorption. In this sense, it is quite natural to adopt $\Phi_{\mathbf{k}}^{(-)}(\mathbf{r};R)$ in Eq. (3) as the electronic scattering state, since $\langle\Phi_{\mathbf{k}}^{(-)}|V_2|\Phi_e\rangle_{\mathbf{r}}$ in Eq. (13) precisely corresponds to Eq. (40). However, Eq. (40) is valid only if Raman–Stokes deactivation can be neglected.

On the other hand, the equations of motion, Eqs. (12) and (13), do not necessarily represent only photoabsorbing electron emission without photoemitting electron recombination, since the appropriate boundary condition has not been imposed. Hence the latter process can mathematically occur in this formalism. Formally, one may be able to remove the incoming spherical components by imposing a stringent condition on $\chi_{\mathbf{k}}(R,t)$, as discussed by Takatsuka.[32] One may also construct a theory, in which both electronic and nuclear motions are represented by time-dependent wave packets, whereby photoelectrons move toward the asymptotic region after photoabsorption.

There are several conventional ways to remedy this situation. For example, one may employ an optical potential that absorbs nuclear wave packets of the ion upon photoabsorption. This approach has a drawback though, since one cannot observe the time propagation of the wave packets nor can the vibrational spectra be extracted from them. An example of such spectra will be shown in Sec. IV C. Here we take a different approach. Let us rewrite Eqs. (34) and (35), omitting the suffices ℓ and m for clarity,

$$i\hbar\frac{\partial}{\partial t}\chi_e = H_e\chi_e + V_{eg}\chi_g + \sum_j \tilde{C}_j^*\tilde{\chi}_j \tag{41}$$

and

$$i\hbar\frac{\partial}{\partial t}\tilde{\chi}_j = (H_i+\varepsilon_j)\tilde{\chi}_j + \tilde{C}_j\chi_e, \tag{42}$$

where $H_i=[T_N+V_{\text{ion}}]$, and $\varepsilon_j=(k_j\hbar)^2/2m$. Absorption of a photon that leads to ionization can readily be detected by looking at the time dependence of the norm within a given interval ΔR in the ionized state such that

$$\frac{d}{dt}\langle\tilde{\chi}_j|\tilde{\chi}_j\rangle_{\Delta R} = \frac{1}{2i\hbar}(\langle\tilde{\chi}_j|\tilde{C}_j\chi_e\rangle_{\Delta R} - \langle\tilde{C}_j\chi_e|\tilde{\chi}_j\rangle_{\Delta R}) = \frac{1}{\hbar}\mathrm{Im}\langle\tilde{\chi}_j|\tilde{C}_j\chi_e\rangle_{\Delta R}, \tag{43}$$

where Im specifies the imaginary part and the integration should be carried out in the range $[R,R+\Delta R]$. If $(d/dt)\times\langle\tilde{\chi}_j|\tilde{\chi}_j\rangle_{\Delta R}$ is negative, the (spurious) deactivation occurs in this domain. Thus the sign of $\mathrm{Im}\langle\tilde{\chi}_j|\tilde{C}_j\chi_e\rangle_{\Delta R}$ monitors the absorption and emission there. This condition can simply be extended so as to be considered in a pointwise manner at a given R by $\Delta R\to 0$, such that $\mathrm{Im}\langle\tilde{\chi}_j|\tilde{C}_j\chi_e\rangle_{\Delta R}\to\Delta R\,\mathrm{Im}(\tilde{\chi}_j^*\tilde{C}_j\chi_e)$. As soon as the deactivation begins at R, or as soon as $\mathrm{Im}(\tilde{\chi}_j^*\tilde{C}_j\chi_e)$ turns negative, the optical interaction between $\tilde{\chi}_j(R)$ and $\chi_e(R)$ should be turned off. This procedure should be applied to each channel (k_j,ℓ,m). We thus modify the equations of motion (41) and (42) such that

$$i\hbar\frac{\partial}{\partial t}\chi_e = H_e\chi_e + V_{eg}\chi_g + \sum_j \tilde{C}_j^*\tilde{\chi}_j\theta[\mathrm{Im}(\tilde{\chi}_j^*\tilde{C}_j\chi_e)] \tag{44}$$

and

$$i\hbar\frac{\partial}{\partial t}\tilde{\chi}_j = (H_i+\varepsilon_j)\tilde{\chi}_j + \tilde{C}_j\chi_e\theta[\mathrm{Im}(\tilde{\chi}_j^*\tilde{C}_j\chi_e)], \tag{45}$$

where $\theta(x)$ is the step function, with a value of 1 for $x=0$ and 0 otherwise. This procedure introduces a nonlinearity in

the equations, thereby causing numerical complexity, and hence, the sign of $\mathrm{Im}(\tilde{\chi}_j^* \tilde{C}_j \chi_e)$ is monitored just one step ahead of each time propagation.

Before applying this switching function, we should note that k_j appearing in the equations of motion can be larger than values corresponding to the photon energy provided by the lasers. These components represent closed channels. The closed channels are, of course, virtual but are necessary to make the expansion of Eq. (3) complete. These closed-channel wave packets have some finite values soon after the probe laser is turned on, and represent some deformation of the nuclear wave functions. They eventually damp to zero. This damping is natural and should not be suppressed by the switching function. It is thus clear that the above switching function should be imposed only on the open channels. We further note that the closing of the channels depends on the nuclear coordinate R. However, it is not trivial to define the closed channel in time-dependent scattering theory, since energy uncertainty is inevitable. We therefore set a very simple criterion to define the open channels, which depends on the nuclear coordinates. Suppose the total (electronic and vibrational) energy of the initial state is E_0. For a state having ε_j as the photoelectron kinetic energy, a wave packet $\tilde{\chi}_j(R)$ is defined to be open if the total electronic energy at this position, i.e., $V_{\mathrm{ion}}(R)+\varepsilon_j$, is smaller than the total energy,

$$\hbar\omega_1+\hbar\omega_2+E_0>V_{\mathrm{ion}}(R)+\varepsilon_j, \tag{46}$$

provided that the energy uncertainty width due to the pulse laser can be ignored. Only when this condition is fulfilled, is the switching function applied.

D. Split-operator technique

The coupled equations of motion for the wave packets can be rewritten in compact form as

$$i\hbar\frac{\partial}{\partial t}\boldsymbol{\chi}(R,t)=\hat{\mathbf{H}}(R,t)\boldsymbol{\chi}(R,t)$$
$$=[\hat{\mathbf{T}}(R)+\mathbf{V}_D(R)+\mathbf{V}_O(R,t)]\boldsymbol{\chi}(R,t). \tag{47}$$

The operators are represented by $N\times N$ matrices, where N can be several hundreds or more depending on the energy and the polarization of the probe laser. $\hat{\mathbf{T}}(R)$ is a diagonal matrix of the kinetic operator, and can be treated by fast fourier transform (FFT) techniques as usual.[33] $\mathbf{V}_D(R)$ is also a diagonal matrix composed of potential surfaces for the ground, excited, and ionized states. All the information about the lasers is contained in the off-diagonal matrix $\mathbf{V}_O(R,t)$, which couples the ground and excited state, and the excited and ionized states which are further decomposed into $(k_j \swarrow m)$ substates. The vector of the wave packets is

$$\boldsymbol{\chi}(R,t)=\begin{pmatrix}\chi_g(R,t)\\ \chi_e(R,t)\\ \chi_{k_j\swarrow m}(R,t)\\ \vdots\end{pmatrix}. \tag{48}$$

We solve these time-dependent coupled equations using the split-operator technique.[33,34] The split-operator technique begins with the Trotter formula for a pair of noncommuting operators $[A,B]$,

$$e^{-t(A+B)}=\lim_{n\to\infty}(e^{-tA/n}e^{-tB/n})^n, \tag{49}$$

and is exact only if $n\to\infty$ can be realized. There are many versions for handling the time-propagation operator within a finite-time scheme, such as the symplectic integrator method.[34] One of the standard techniques, which we use here, takes the following decomposition for a small time increment $\Delta t=t/n$,

$$e^{-\Delta t(A+B)}\approx e^{-\Delta tA/2}e^{-\Delta tB}e^{-\Delta tA/2}. \tag{50}$$

The split-operator technique is well established for a scalar potential surface. One can extend this to the vector problem. We have also devised an efficient method to diagonalize $V_O(R,t)$ analytically, which drastically shortens this process that is otherwise very time-consuming. Our procedure can be compactly described in terms of the following operator ordering:

$$\boldsymbol{\chi}(R,t+\Delta t)=\exp\left(-\frac{i\Delta t}{\hbar}\hat{H}(R,t)\right)\boldsymbol{\chi}(R,t)$$
$$=\exp\left(-\frac{i\Delta t}{2\hbar}[\hat{T}(R)+V_D(R)]\right)\exp\left(-\frac{i\Delta t}{\hbar}V_O(R,t)\right)\exp\left(-\frac{i\Delta t}{2\hbar}[\hat{T}(R)+V_D(R)]\right)\boldsymbol{\chi}(R,t)$$
$$=\exp\left(-\frac{i\Delta t}{4\hbar}V_D(R)\right)\exp\left(-\frac{i\Delta t}{2\hbar}\hat{T}(R)\right)\exp\left(-\frac{i\Delta t}{4\hbar}V_D(R)\right)\exp\left(-\frac{i\Delta t}{\hbar}V_O(R,t)\right)\exp\left(-\frac{i\Delta t}{4\hbar}V_D(R)\right)$$
$$\times\exp\left(-\frac{i\Delta t}{2\hbar}\hat{T}(R)\right)\exp\left(-\frac{i\Delta t}{4\hbar}V_D(R)\right)\boldsymbol{\chi}(R,t). \tag{51}$$

In each time step Δt, one diagonalization and two sets of FFT's and associated inverse FFT's must be carried out.

To prepare an eigenfunction on the ground potential surface which serves as an initial wave packet, we apply the energy screening technique.[35] This technique extracts the eigenfunctions directly from wave packet dynamics such that

$$\Delta(E_1,E_2)\chi(0) = \int_{E_1}^{E_2} \delta(E-T_N-V_g)\chi(0)dE = (2\pi)^{-1}\int_{-\infty}^{\infty} dt\,\frac{1}{it}\left[\exp\left(\frac{i}{\hbar}E_2 t\right)-\exp\left(\frac{i}{\hbar}E_1 t\right)\right]\chi(t). \tag{52}$$

$\Delta(E_1,E_2)$ is a projection operator that picks the eigenfunctions from an arbitrary energy interval $[E_1,E_2]$. If the interval includes only one eigenstate, this projection operator produces the corresponding eigenfunction. This technique is particularly useful when a highly excited eigenstate is chosen as the initial wave packet.

III. ELECTRONIC STRUCTURE AND PHOTOIONIZATION AMPLITUDES

Figure 1 shows the potential energy curves for the ground $X\,^1\Sigma_g^+$ and double-minimum $^1\Sigma_u^+$ states of neutral Na_2 and the ground $X\,^2\Sigma_g^+$ state of the Na_2^+ ion and illustrates our pump–probe scheme. The double-minimum $^1\Sigma_u^+$ state has been studied extensively, and results from an avoided crossing of two adiabatic states. The inner well is a Rydberg state with a principal configuration of $\sigma_g(3s)\sigma_u(4s)$ and the outer well is a strong admixture of the $\sigma_g(4s)\sigma_u(3s)$ and $\sigma_g(3s)\sigma_u(3s)$ configurations. The $\sigma_g(3s)\sigma_u(3s)$ configuration lends significant ionic character to this state.

The electronic wave functions and energies for the ground states of Na_2 and Na_2^+ were obtained from extensive configuration-interaction (CI) studies using the GAMESS package. Calculations were done at 19 internuclear distances between 2 and 11 Å. For convenience in the calculation of the dipole matrix elements between the ground and excited states and for photoionization of the excited state, we employed the Hartree–Fock (HF) basis of the ion in these CI calculations. For a more accurate description of the excited state, we adopt the rotationless experimental potential of Cooper *et al.*[36] in the wave packet calculations. All potential curves were adjusted to the known excitation energies and ionization potential.

Figure 1 shows the dipole amplitude between the ground and excited (2) $^1\Sigma_u^+$ states of Na_2. While around the inner well (Rydberg) region, the dipole amplitude is very flat, indicating Franck–Condon behavior, and the dipole amplitude changes substantially in the outer well (ionic) region, reflecting the ionic character of the system.

To obtain the photoionization amplitudes, we used our CI wave function for the double-minimum state and a frozen-core Hartree–Fock (FCHF) description of the wave function for the ionized state. For the FCHF model the wave function is taken to be an antisymmetrized product of HF ion orbitals and a photoelectron orbital that is a solution of a one-electron Schrödinger equation containing the Hartree–Fock potential of the ion core. The HF wave function provides a very adequate description of Na_2^+ over all internuclear distances of interest.

The $C_{\ell m}$ coefficients of Eq. (22) incorporate the underlying dynamics into our formulation of time-resolved photoelectron spectroscopy. These $C_{\ell m}$ coefficients for polarization vectors of the pump and probe pulses parallel to the molecular axis and for a photoelectron energy of about 0.6 eV are shown as a function of internuclear distance in Fig. 1. For this state of Na_2 only even ℓ's arise, while for this parallel arrangement only $m=0$ terms are allowed. These $C_{\ell m}$'s display several important features. Among these, we note the striking change in the $C_{\ell m}$'s in the barrier region where the avoided crossing occurs. This behavior could be expected to be quite general in regions of nonadiabatic behavior. Furthermore, the large magnitude of these $C_{\ell m}$'s around the barrier will exert a strong influence on the ion signal as the wave packet moves through this region. The pronounced oscillatory behavior of these coefficients for all ℓ's ($\ell=0$, 2, and 4 are shown) arises from the evolution of the electronic structure in the outer well where the wave function acquires significant ionic character. These features reflect non-Franck–Condon behavior of the underlying photoelectron matrix elements. Such behavior should arise quite generally in nonadiabatic regions of potential surfaces and, in fact, have been seen in the NaI system.[29]

IV. WAVE PACKET DYNAMICS OF Na_2

We have used the formulation, potential curves (see Fig. 1), and photoionization amplitudes outlined in the previous sections to study the pump–probe photoelectron spectra in Na_2. Important parameters in these studies include,

(a) All potential energies are measured from the bottom of V_g. The initial wave packet $\chi_g(0)$ is the vibrational ground state of V_g with energy $E_{\text{ground}}=9.3509\times10^{-3}$ eV.

(b) The characteristic points of the potential curves are as follows: The local minimum of the inner well of V_e lies at $R=3.7$ Å and 3.589 eV, while that of the outer well is at 6.7 Å and 3.518 eV. The barrier between them lies at $R=4.7$ Å and 3.6753 eV, resulting in a barrier height of 0.0873 eV from the bottom of the inner well. The ion potential curve has its minimum at $R=3.6$ Å and 5.064 eV.

(c) The laser parameters: We examine three different photon energies for the pump laser of 3.6192, 3.6763, and 3.7007 eV resulting in a wave packet on V_e below the barrier, at the top of the barrier, and above the barrier, respectively. The electric field strength and the full width at half maximum (FWHM) of the Gaussian pulses were taken to be $5.142\,83\times10^6$ eV/m (0.001 au) and 100 fs, respectively.

(d) The probe laser is fixed for all the above cases at

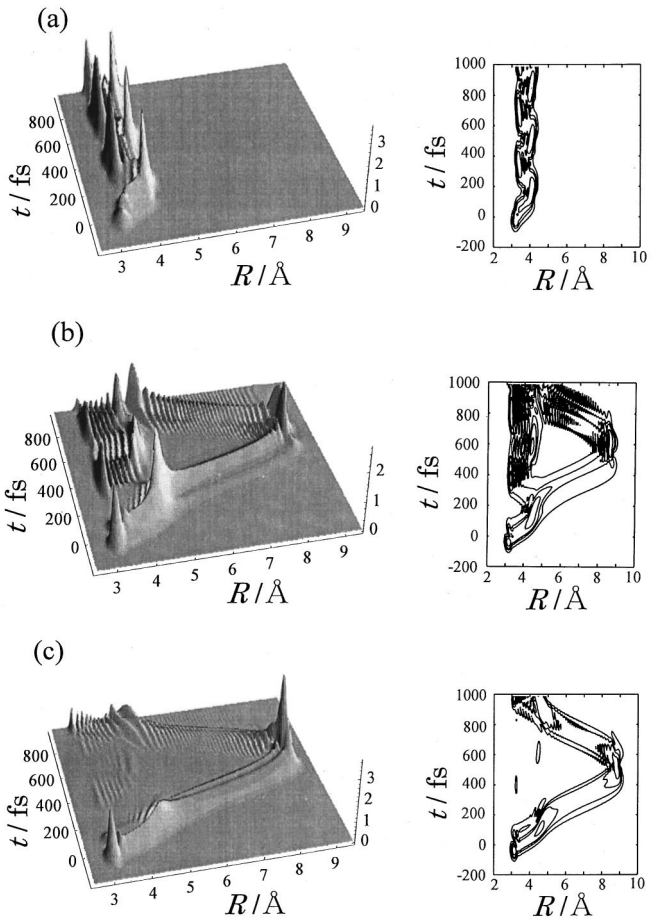

FIG. 3. Perspective view and contour plot of the absolute square of the wave packets, $|\chi_e(R,t)|^2$ generated by the pump lasers with (a) $\hbar\omega_1 = 3.6192$ eV (below the barrier), (b) $\hbar\omega_1 = 3.6763$ eV (at the barrier), and (c) $\hbar\omega_1 = 3.7007$ eV (above the barrier).

$\hbar\omega_2 = 2.2776$ eV, $E_{02} = 1.028\,57 \times 10^8$ eV/m, and FWHM = 40 fs. These values were chosen to give large gains in the photoionization signals.

(e) The molecular orientation is parallel to the pump laser, that is $\theta_R = 0°$. For each of these three ω_1, the polarization vector of the probe laser is set either parallel or perpendicular to the molecular axis.

The $|\chi_e(R,t)|^2$ for the wave packets on the excited state are shown in Figs. 3(a)–3(c), and for pump photon energies below the barrier, at the barrier, and above the barrier, respectively. For a pump energy below the barrier, the $\chi_e(R,t)$ is clearly confined to the inner well [Fig. 3(a)]. For a pump photon energy at the barrier, the wave packet bifurcates in the barrier region with one component proceeding to the outer well after some slowing down over the barrier, while the other component is reflected back into the inner well [Fig. 3(b)]. For a pump photon energy above the barrier, the wave packet mostly passes over the barrier and moves into the outer well [Fig. 3(c)].

To discretize the equations of motion, Eqs. (34) and (35), we approximate the integral over k in the total scattering wave function by a Gaussian quadrature. Since the computational effort scales rapidly with the number of quadrature points (N_k), it is important to obtain converged solutions of the coupled equations with sufficiently small values of N_k and we have therefore examined the convergence of these solutions with N_k carefully. Figure 4 shows some typical results of these convergence studies of the photoelectron signal with N_k. Shown here are angular momentum components of the photoelectron signal, $P_{\ell m}(\varepsilon_{k_j})$,

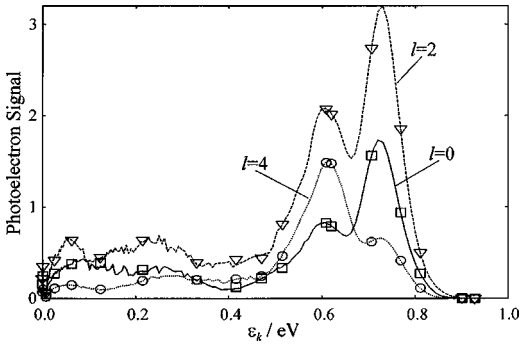

FIG. 4. Illustration of the convergence of the quadrature for integration over k. The partial waves for $\ell = 0$, 2, 4 and with $m = 0$ are examined. The pointwise values represent the results of a 14-point Gauss–Legendre scheme augmented with a 7-point Gauss–Hermite one, while the smooth curves are from a 299-point Simpson rule.

$$P_{\ell m}(\varepsilon_{k_j}) = \frac{m_e}{\hbar^2} k_j \int dR |\chi_{k_j \ell m}(R,t_f)|^2, \tag{53}$$

where ε_k is the photoelectron energy and t_f is a long time after the probe is switched off. These $P_{\ell m}$'s are for a pump pulse which just puts the wave packet at the top of the barrier and for a pump–probe delay time of 242 fs. The polarization vectors of the pump and probe pulses are also parallel to the molecular axis. The smooth curves in Fig. 4 were obtained with a 299-point Simpson rule. The pointwise data shown in Fig. 4 are results with a 14-point Gauss–Legendre quadrature augmented by a 7-point Gauss–Hermite scheme chosen to improve the quadrature around $\varepsilon_k = 0.7$ eV. Agreement between this 21-point Gauss quadrature and 299-point Simpson calculations is very good and we have hence used this 21-point quadrature in these studies.

A. Oscillatory photoelectron signal

The non-Franck–Condon behavior of the photoionization amplitudes for this double-minimum state of Na_2 is evident in the oscillatory behavior of the $C_{\ell m}$ coefficients with internuclear geometry. An unusual consequence of this behavior of the $C_{\ell m}$'s arises from their near-vanishing values for all (k_j, ℓ, m) in a narrow range to the left ($R \cong 4.1$ Å) of the potential barrier on the excited state. One may thus predict that a wave packet placed inside the inner potential well should exhibit a very small photoelectron signal whenever the wave packet hits this ''depleted'' region. This should result in an oscillatory behavior of the total photoelectron signal as a function of delay time. This behavior is seen in the ion signal of Fig. 5 for a pump pulse of energy 3.6192 eV which places the wave packet in the inner well and for the polarization vectors of the pump and probe pulses parallel to the molecular axis. The rapidly oscillating solid line represents the total ion signal given by

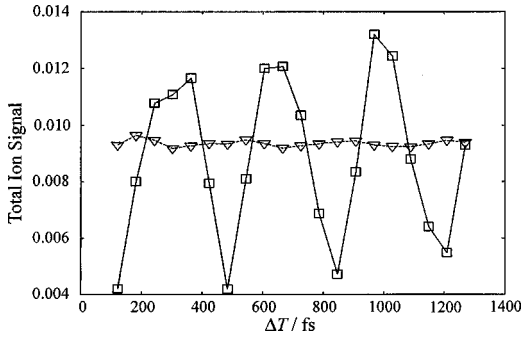

FIG. 5. Oscillatory behavior of the total ion signal (solid line) arising from the wave packet confined in the inner potential basin. Broken line: the total ion signal based on the Franck–Condon approximation.

$$P_{\text{ion}} = \int \sum_{\ell,m} P_{\ell m}(\varepsilon_k)\, d\varepsilon_k = \int P(\varepsilon_k)\, d\varepsilon_k . \tag{54}$$

Upon excitation this wave packet immediately begins an oscillatory motion of period about 347 fs, hitting the right-hand-side turning point in the inner well near 4.1 Å at $t = 158$, 505, 842, and 1180 fs, where the ion signal has minima. The signal at these minima gradually becomes larger due to dispersion of the wave packet.

To further highlight this unusual behavior, we have calculated the total ion signal for ionization of these wave packets, but with the Franck–Condon approximation, where $C_{20}(k_j, R)$, the largest of these coefficients, is simply replaced by its constant value at $R = 3.5$ Å at each photoelectron energy and all other $C_{\ell m}(k_j, R)$'s are set to zero. The dotted flat line in Fig. 5 shows the result. The difference is striking and illustrates the importance of the underlying photoionization dynamics to a mapping of the wave packet via pump–probe photoelectron spectra.

B. Energy-resolved photoelectron signals

We next examine the kinetic energy distribution of the photoelectrons, $P(\varepsilon_k)$. As stated previously, three pump energies were studied with parallel and perpendicular polarizations. Figures 6(a)–6(c) show these $P(\varepsilon_k)$ as a function of delay time for pump photons that place the wave packet in the inner well, on top of the barrier, and above the barrier for parallel polarizations of the pump and probe pulses. Figures 6(A)–6(C) show the spectra for perpendicular orientations of the pump and probe pulses. The only significant difference between these parallel and perpendicular cases is in the magnitudes of the signals. When the wave packet is confined to the inner well [Fig. 3(a)], the major feature of the photoelectron spectra is a strong peak around 0.7 eV [Figs. 6(a) and 6(A)] which shows an oscillatory dependence on the pump–probe delay time, as discussed above. This feature is clearly a fingerprint of the localization of the wave packet in the inner well.

When the pump photon places the wave packet on top of the barrier, the photoelectron spectra [Figs. 6(b) and 6(B)] behave quite differently. At about $\Delta T = 200$ fs, the wave packet is moving slowly through the barrier region [Fig. 3(b)], where the photoionization amplitudes are large (Fig. 1). This results in a strong peak at around 0.7 eV. In this region the wave packet bifurcates into a component that moves into the outer well and another that is reflected back

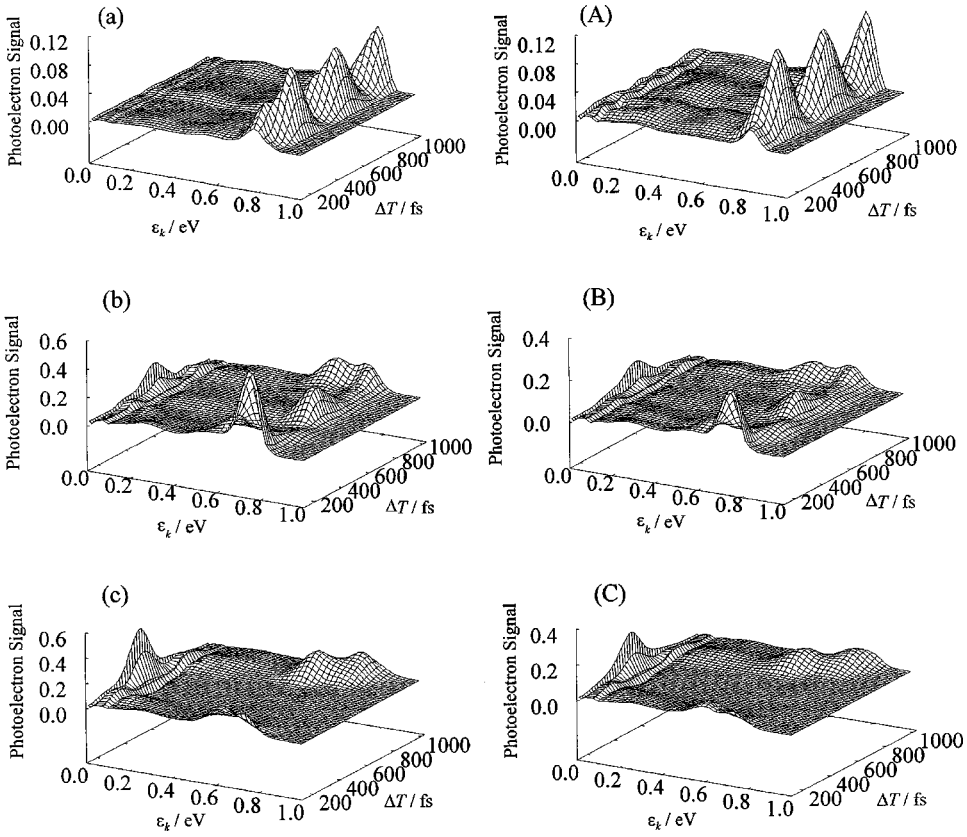

FIG. 6. Photoelectron signal $P(\varepsilon_k)$ vs kinetic energy and delay time. The photon energy of the pump laser is (a), (A) $\hbar\omega_1 = 3.6192$ eV (below the barrier), (b), (B) $\hbar\omega_1 = 3.6763$ eV (at the barrier), and (c), (C) $\hbar\omega_1 = 3.7007$ eV (above the barrier). For each energy, the polarization vector of the probe laser is set parallel [(a), (b), (c)] and perpendicular [(A), (B), (C)] to that of the pump laser. Note that the vertical scales are different for different energies.

to the inner well. The period of recurrence of the wave packet in the inner well happens to be about half of that of its outer-well counterpart. At about $\Delta T = 600$ fs, the outer-well component reaches its turning point, which results in a strong peak in the photoelectron signal at very low kinetic energy. This feature was first pointed out by Meier and Engel,[16,17] who also noted its value for mapping wave packets at their turning points. On the other hand, the inner wave packet, which becomes rather dispersed, leads to a peak at about $\varepsilon_k = 0.7$ eV at $\Delta T = 600$ fs. An interesting double-peak feature is seen around $\varepsilon_k = 0.7$ eV and $\Delta T = 1000$ fs. We will return to this feature in the next subsection.

When the pump pulse places the wave packet above the barrier, the photoelectron spectra are simpler [Figs. 6(c) and 6(C)], since no major bifurcation of the wave packet occurs at the potential barrier. As in the other cases, the peak around $\varepsilon_k = 0.7$ eV arises from the wave packet while it is in the inner well. Once over the barrier, this peak at 0.7 eV is no longer present, reflecting the absence of any major component in the inner well [Fig. 3(c)]. A high peak at a very low photoelectron energy around $\Delta T = 500$ fs again arises at the outer turning point. The broad feature at $\varepsilon_k = 0.7$ eV and $\Delta T = 800-1000$ fs is due to the dispersed wave returning to the inner well.

C. Relationship between vibrational and photoelectron spectra

The vibrational spectrum, $S(E_v)$, extracted from the ion wave packets $\chi_{\mathbf{k}}$, provides complementary information to the energy-resolved photoelectron spectra. This spectrum is obtained from

$$S(E_v) = \int dk k^2 \sum_{\ell,m} \int ds \int dR \chi^*_{k\ell m}(R,t_f,\Delta T) \times \chi_{k\ell m}(R,t_f+s;\Delta T)\exp\left(\frac{i}{\hbar}E_v s\right), \tag{55}$$

where E_v (measured from the bottom of V_g) is the energy associated with molecular vibration. Figure 7 shows $S(E_v)$ for the case of a pump photon with energy close to the top of the barrier and for parallel polarization of the pump and probe pulses, at selected delay times $\Delta T = 121$, 242, 605, and 968 fs. The global features of this vibrational spectrum are rather similar to the photoelectron spectra shown in Fig. 6(b). Starting from a single major feature located around $E_v = 5.2$ eV at $\Delta T = 121$ fs, $S(E_v)$ splits into two major peaks at $E_v = 5.2$ and 5.35 eV at a delay time of $\Delta T = 242$ fs. The higher-energy group disappears at $\Delta T = 605$ fs. At a delay time of 968 fs two peaks reappear, with one of these shifted to slightly lower energy.

From energy conservation, we expect

$$E_v + \varepsilon_k = \hbar(\omega_1 + \omega_2) + E_{\text{ground}} \equiv E_{\text{tot}}, \tag{56}$$

where E_{ground} is the energy of the initial state prepared on V_g. While this equality is not rigorous due to the uncertainty principle unless a stationary optical source is used, the following relation may apply:

$$S(E_v) \propto P(E_{\text{tot}} - E_v). \tag{57}$$

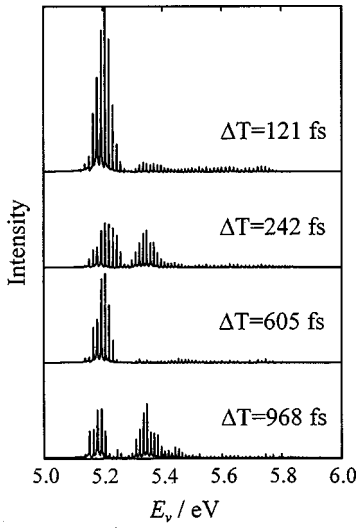

FIG. 7. Vibrational spectra of the Na_2 cation at selected delay times for the case of a pump energy at the top of the barrier and parallel polarization.

Figure 8 shows plots of $S(E_v)$ and $P(E_{\text{tot}} - E_v)$ for $E_{\text{tot}} = 5.9633$ eV. For convenience, we have simply connected the available values of $P(E_{\text{tot}} - E_v)$ with straight lines in Fig. 8. The overall consistency is evident. However, we do note the absence of a peak in $S(E_v)$ at $E_v \simeq E_{\text{tot}}$ and 605 fs, where a strong peak is seen at very low energy in the photoelectron spectrum [cf. Fig. 6(b)]. This low-energy peak in $P(\varepsilon_k)$ arises when the wave packet hits the outer turning point.[16,17] This difference between $S(E_v)$ and $P(E_{\text{tot}} - E_v)$ at the low ε_k is due to the definition of $P(\varepsilon_k)$. Writing P_{ion} as

$$P_{\text{ion}} = \int P(\varepsilon_k) d\varepsilon_k = \int dk k^2 \sum_{\ell m} \int dR |\chi_{k\ell m}(R,t_f)|^2 = \int P(\varepsilon_k) \frac{\hbar^2 k}{m_e} dk, \tag{58}$$

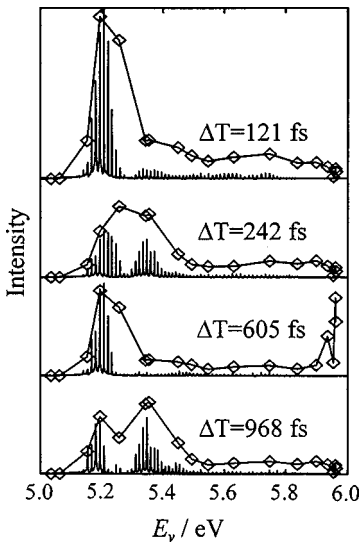

FIG. 8. Comparison of $P(E_{\text{tot}} - E_v)$ for $E_{\text{tot}} = 5.9633$ eV with the vibrational spectrum $S(E_v)$ of Fig. 7.

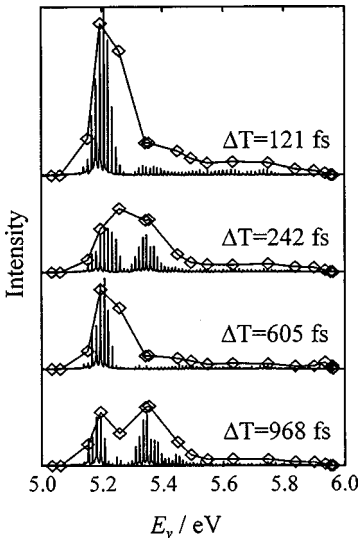

FIG. 9. Comparison of $kP(E_{\rm tot}-E_v)$ with $E_{\rm tot}=5.9633$ eV and the vibrational spectrum $S(E_v)$ of Fig. 7.

and comparing this with $S(E_v)$ in Eq. (55), one sees that Eq. (57) should be replaced by

$$S(E_v)\propto \frac{\hbar^2 k}{m_e} P(E_{\rm tot}-E_v) \tag{59}$$

with

$$k=\frac{\sqrt{2m_e}}{\hbar}\sqrt{E_{\rm tot}-E_v}\,. \tag{60}$$

In fact, the overall agreement between $kP(E_{\rm tot}-E_v)$ and $S(E_v)$ is far better, as shown in Fig. 9.

Comparison of $S(E_v)$ and $kP(E_{\rm tot}-E_v)$ may suggest that the strong feature centered at $E_v=5.2$ eV arises from the wave packet moving in the inner well, while the feature at $E_v=5.35$ eV must be associated with the wave packet component moving in the outer well. However, it is not quite clear how these values in E_v would arise. The origin of the vibrational feature around $E_v=5.35$ eV is more difficult to understand, since the potential curve of the ion at $R\geqslant 5.6$ Å lies above 5.5 eV (see Fig. 1). For example, at $R=6.7$ Å, which is the bottom of the outer well, $V_{\rm ion}(R)$ is about 5.8 eV, and there is hence no way for a wave packet lying there to be in a vibrational state at $E_v=5.35$ eV. It is more reasonable therefore to assume that these large features must be due to two large ionization amplitudes $C_{\ell m}(k_j,R)$, at, say, $R^*_{\rm in}$ and $R^*_{\rm out}$, just sandwiching the potential barrier on $V_e(R)$ (see Fig. 1). As a wave packet passes through the barrier region, its kinetic energy is small enough to remain there for a longer time, which allows the packet to acquire a larger ionization probability. Furthermore, assuming that a wave packet does not change its momentum upon ionization from $V_e(R)$ to $V_{\rm ion}(R)$ at each R, in accordance with the Condon approximation, then a wave packet passing through these two high peaks at $R^*_{\rm in}$ and $R^*_{\rm out}$ should be promoted to energies close to $E_v=5.20$ and 5.35 eV, respectively.

It is worth noting that in their pump–probe studies of $Na_2(X\,^1\Sigma_g^+)\rightarrow Na_2(^1\Sigma_u^+)\rightarrow Na(3s)+Na^+$, Baumert *et al.*[37] observed an oscillatory signal of Na^+ transient as a function of the delay-time ΔT. They found that the Fourier transform of this signal with respect to the delay time yielded the basic frequency for coherent motion of the wave packet on the double-minimum state $^1\Sigma_u^+$, and, moreover, emphasized that the Fourier spectrum so obtained is composed of individual frequencies corresponding to the energy spacings of the vibrational levels forming the wave packet. This vibrational feature should arise directly from $\chi_e(R,t)$. Though our spectra taken as in Eq. (55) pertain to the vibrational motion of the wave packet of the product ion Na_2^+, or $\chi_{k\ell m}(R,t_f+s;\Delta T)$, these results do confirm that information about vibrational states can indeed be obtained from pump–probe photoelectron spectroscopy.

D. Angular distribution of photoelectrons

In conventional photoelectron spectroscopy, angular distributions are known to provide valuable insight into the underlying dynamics. A few groups have, moreover, recently reported measurements of angular distributions in pump–probe photoelectron spectra.[24–26] Althorpe and Seideman have also examined the angular distributions of photoelectrons in the pump–probe ionization for a rigid diatomic molecule NO.[38] We have also recently published a brief report on photoelectron angular distributions for pump–probe ionization of aligned Na_2.[27]

These time-resolved photoelectron angular distributions are given by

$$A(\theta_k,\Delta T) = \int dk k^2 \int dR \left| \sum_{\ell,m} \chi_{k\ell m}(R,t_f;\Delta T) Y_{\ell m}(\theta_k,\phi_k) \right|^2, \tag{61}$$

where ϕ_k is set to zero. Figure 10 shows a few such photoelectron spectra for pump photon energies below, on top of, and over the barrier in the excited state. In contrast to the kinetic energy distributions in Fig. 6, these angular distributions are significantly different for the parallel and perpendicular cases. For the parallel case, the angular distribution is generally of d_{z^2} type, as illustrated by the inset of Fig. 10, while it is basically of d_{yz} type for the perpendicular case. These shapes are expected on the basis of symmetry considerations for a dipole interaction. The oscillatory behavior of these angular distributions with time when the wave packet is in the inner well (Fig. 10) simply reflect the oscillation of the ion signal seen in Fig. 5 and discussed previously. The main difference in the angular distributions for the cases when the pump photon places the packet just at or above the barrier is the absence of the peak for a delay time of 600 fs in the latter case. This difference arises from the fact that in the latter case the wave packet has virtually no inner-well component until the wave packet returns there from the outer well at around 800 fs.

The dependence of these photoelectron angular distributions on the orientation of polarization of the probe and the molecular axis can potentially be exploited to monitor molecular rotation. Such use of pump–probe photoelectron angular distributions for real-time mapping of molecular rota-

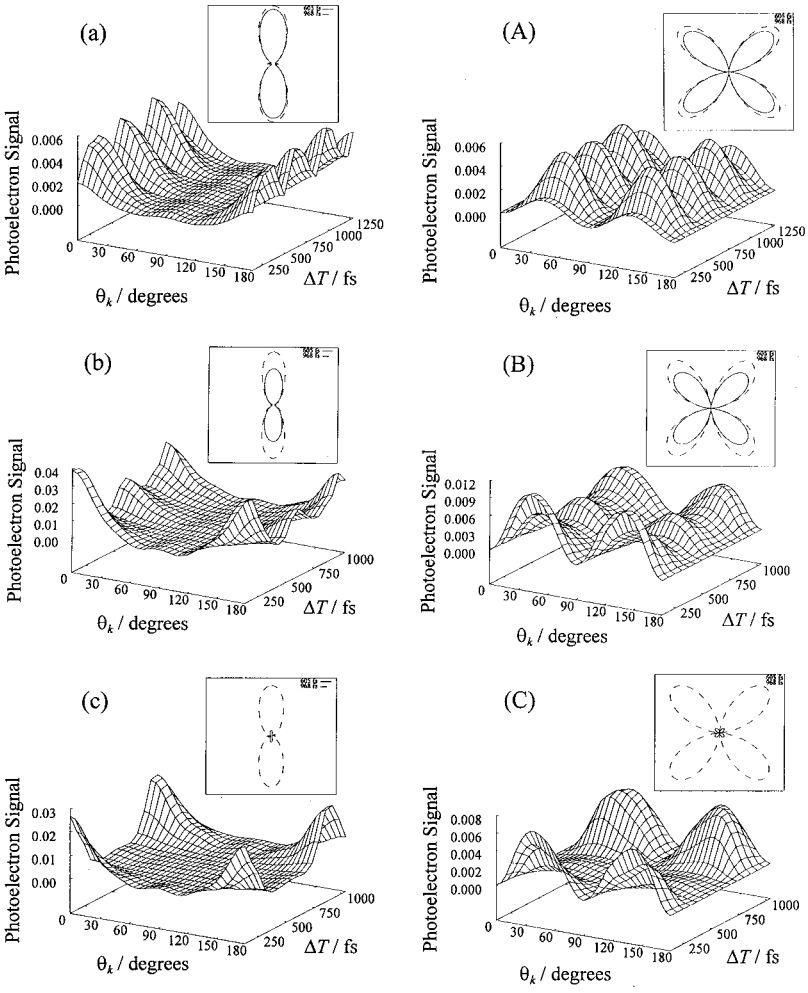

FIG. 10. The photoelectron angular distributions as a function of the delay time. As in Fig. 6, the photon energy of the pump laser is (a), (A) $\hbar\omega_1 = 3.6192$ eV (below the barrier), (b), (B) $\hbar\omega_1 = 3.6763$ eV (at the barrier), and (c), (C) $\hbar\omega_1 = 3.7007$ eV (above the barrier). For each energy, the polarization vector of the probe laser is set parallel and perpendicular to that of the pump field. The insets show a polar coordinate representation of $A(\theta_k, \Delta T)$ at $\Delta T = 605$ fs (broken curves) and 968 fs (smooth lines).

tion can be a valuable supplement or alternative to laser induced fluorescence (LIF) detection.[3] For example, consider a case where the polarization vector of the pump and probe pulses are parallel to the *z*-axis and the molecule lies in the *yz* plane (Fig. 2). If the molecular axis lies along θ_R at the time of probing (ΔT), the angular distribution is given as

$$A(\theta_k : \theta_R(\Delta T)) = \cos^2\theta_R \times (d_{z^2}\text{-type distribution}) + \sin^2\theta_R \times (d_{yz}\text{-type distribution}) + \cos\theta_R \sin\theta_R (\text{cross term}), \quad (62)$$

and the photoelectron signal depends strongly on the position of the detector. The actual signals should, of course, be convoluted over the vibrational motion. This aspect will be discussed in greater detail in a future publication.[31]

V. CONCLUDING REMARKS

The results of these studies illustrate several key points. First, while a robust description of the underlying photoionization amplitudes can generally enhance the utility of femtosecond pump–probe photoelectron spectra as a probe of wave packet dynamics and of the evolution of electronic structure, use of such photoionization amplitudes and their dependence on geometry is quite essential to unraveling wave packet dynamics from photoelectron signals in nonadiabatic regions. Studies of femtosecond photoelectron spectra for wave packet motion in NaI underway provide further and compelling evidence of this. Second, photoelectron angular distributions not only provide insightful fingerprints of vibrational wave packet dynamics, but their strong dependence on the relative orientation of the pump and probe polarizations can also be exploited to monitor real-time molecular rotation.

ACKNOWLEDGMENTS

This work has been supported by a grant from the Ministry of Education, Science, and Culture (Japan), and the National Science Foundation (U.S.).

[1] A. H. Zewail, *Femtochemistry: Ultrafast Dynamics of the Chemical Bond* (World Scientific, Singapore, 1994), Vols. 1 and 2.
[2] *Femtosecond Chemistry*, edited by J. Manz and L. Wöste (VCH, Weinheim, 1995).
[3] M. Dantus, R. M. Bowman, and A. H. Zewail, Nature (London) **343**, 737 (1990).
[4] W. R. Lambert, P. M. Felker, and A. H. Zewail, J. Chem. Phys. **75**, 5958 (1981).
[5] T. S. Rose, M. J. Rosker, and A. H. Zewail, J. Chem. Phys. **88**, 6672 (1988).
[6] *Femtochemistry: Ultrafast Chemical and Physical Processes in Molecular Systems*, edited by M. Chergui (World Scientific, Singapore, 1996).
[7] *Chemical Reactions and their Control on the Femtosecond Time Scale*, XXth Solvay Conference on Chemistry, edited by P. Gaspard, I. Burghard, I. Prigogine, and S. A. Rice, Adv. Chem. Phys. **101** (Wiley, New York, 1997).

[8] T. Baumert, J. L. Herek, and A. H. Zewail, J. Chem. Phys. **99**, 4430 (1993).
[9] T. Baumert and G. Gerber, Adv. At. Mol., Opt. Phys. **35**, 163 (1995).
[10] H. Ruppe, S. Rutz, E. Schreiber, and L. Wöste, Chem. Phys. Lett. **257**, 356 (1996).
[11] H. Schwoerer, R. Pausch, M. Heid, V. Engel, and W. Kiefer, J. Chem. Phys. **107**, 9749 (1997).
[12] D. Zhong and A. H. Zewail, J. Phys. Chem. **102**, 4031 (1998).
[13] J. M. Smith, X. Zhang, and J. L. Knee, J. Phys. Chem. **99**, 1768 (1995).
[14] M. Seel and W. Domcke, Chem. Phys. **151**, 59 (1991).
[15] M. Seel and W. Domcke, J. Chem. Phys. **95**, 7806 (1991).
[16] Ch. Meier and V. Engel, Chem. Phys. Lett. **212**, 691 (1993).
[17] Ch. Meier and V. Engel, J. Chem. Phys. **101**, 2673 (1994).
[18] M. Braun, Ch. Meier, and V. Engel, J. Chem. Phys. **105**, 530 (1996).
[19] A. Assion, M. Geisler, J. Helbing, V. Seyfried, and T. Baumert, Phys. Rev. A **54**, R4605 (1996).
[20] I. Fischer, D. M. Villeneuve, M. J. J. Vrakking, and A. Stolow, J. Chem. Phys. **102**, 5566 (1995).
[21] C. Jouvet, S. Martrenchard, D. Solgadi, C. Dedonder-Lardeux, M. Mons, G. Grégoire, I. Dimicoli, F. Piuzzi, J. P. Visticot, J. M. Mestdagh, P. D'Oliveira, P. Meynadier, and M. Perdrix, J. Phys. Chem. A **101**, 2555 (1997).
[22] E. Charron and A. Suzor-Weiner, J. Chem. Phys. **108**, 3922 (1998).
[23] J. A. Davies, J. E. LeClaire, R. E. Continetti, and C. C. Hayden, J. Chem. Phys. **111**, 1 (1999).
[24] See, however, E. Charron and A. Suzor-Weiner, J. Chem. Phys. **108**, 3922 (1998), where an empirical form is assumed for the *R*-dependence of the photoionization matrix element.
[25] K. L. Reid, T. A. Field, M. Towrie, and P. Matousek, J. Chem. Phys. **111**, 1438 (1999).
[26] T. Suzuki, L. Wang, and H. Kohguchi, J. Chem. Phys. **111**, 4859 (1999).
[27] Y. Arasaki, K. Takatsuka, K. Wang, and V. McKoy, Chem. Phys. Lett. **302**, 363 (1999).
[28] See, for example, M. Gruebele and A. Zewail, J. Chem. Phys. **98**, 883 (1993).
[29] Y. Arasaki, K. Takatsuka, K. Wang, and V. McKoy (to be published).
[30] R. R. Lucchese, D. K. Watson, and V. McKoy, Phys. Rev. A **22**, 421 (1980); R. R. Lucchese, G. Raseev, and V. McKoy, *ibid.* **25**, 2572 (1982); S. N. Dixit and V. McKoy, J. Chem. Phys. **82**, 3546 (1985); R. R. Lucchese, K. Takatsuka, and V. McKoy, Phys. Rep. **131**, 147 (1986); K. Wang and V. McKoy, J. Chem. Phys. **95**, 4977 (1991); Annu. Rev. Phys. Chem. **46**, 275 (1995).
[31] Y. Arasaki, K. Takatsuka, K. Wang, and V. McKoy (in preparation).
[32] K. Takatsuka, Phys. Rev. A **55**, 347 (1997).
[33] D. Kosloff and R. Kosloff, J. Comput. Phys. **52**, 35 (1983); R. Kosloff, J. Phys. Chem. **92**, 2087 (1988).
[34] K. Takahashi and K. Ikeda, J. Chem. Phys. **99**, 8680 (1993).
[35] K. Takatsuka and N. Hashimoto, J. Chem. Phys. **103**, 6057 (1995).
[36] D. L. Cooper, R. F. Barrow, J. Verges, C. Effantin, and J. D. Incan, Can. J. Phys. **62**, 1543 (1984).
[37] T. Baumert, R. Thalweiser, V. Weiss, and G. Gerber, *Femtosecond Chemistry*, edited by J. Manz and L. Wöste (VCH, Weinheim, 1995), Chap. 12.
[38] S. C. Althorpe and T. Seideman, J. Chem. Phys. **110**, 147 (1999).